

# DeepView: Visualizing the behavior of deep neural networks in a part of the data space

Alexander Schulz, Fabian Hinder, and Barbara Hammer

Cognitive Interaction Technology (CITEC)  
Bielefeld University  
Inspiration 1, D-33619 Bielefeld, Germany  
{schulz,fhinder,bhammer}@techfak.uni-bielefeld.de

June 27, 2022

## Abstract

Machine learning models using deep architectures have been able to implement increasingly powerful and successful models. However, they also become increasingly more complex, more difficult to comprehend and easier to fool. So far, mostly methods have been proposed to investigate the decision of the model for a single given input datum. In this paper, we propose to visualize a part of the decision function of a deep neural network together with a part of the data set in two dimensions with discriminative dimensionality reduction. This enables us to inspect how different properties of the data are treated by the model, such as multimodality, label noise or biased data. Further, the presented approach is complementary to the mentioned interpretation methods from the literature and hence might be even more useful in combination with those.

## 1 Introduction

The increasing relevance of methods of AI in diverse areas such as autonomous driving, algorithmic trading, medical diagnoses, or recommender systems is accompanied by a high potential of vulnerability of these technologies: their use in every-day life in possibly non-stationary environments violates basic assumptions of learning theory such as samples being i.i.d. [16, 14]; adversarial attacks or poisoning can lead to unpredicted behavior of a single decision or the whole model behavior [4, 9]; and skewed sampling of training data can lead to severely biased or unfair machine learning models if no filtering takes place [13]. In combination with legal requirements such as the European Union’s general data protection regulation and right of explanation, these issues have led to a recent boost of explainable AI [17], including sparse local explanations [19], causal modeling [1], counterfactual reasoning [23], feature relevance determination, or saliency maps [20], to name just a few approaches. These methods are accompanied by first approaches how to quantify what means interpretability by humans [12].

Yet, many techniques focus on single decisions rather than displaying parts of the decision boundary and the network’s generalization behavior in the input space. Up to now, there has been comparably little effort to build on human’s astonishing visual perception abilities and to display the behavior of deep networks in a visual plot, which generalizes an extremely natural and intuitive visualization of classification prescriptions: a scatter plot. This is always used in standard textbooks of pattern recognition to explain a classification prescription, it even made it to the cover image in [21]. Yet a method to compute scatter plots, displaying training data, enriched by the decision boundary and network confidence in the plane, does not yet exist for deep networks in high dimensional input space. Indeed, high dimensionality constitutes the major obstacle,

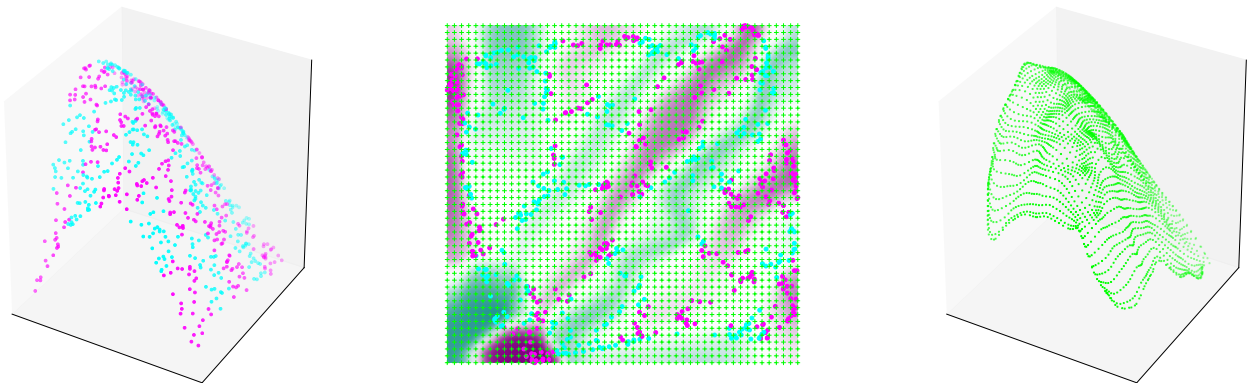


Figure 1: Illustration of the proposed method DeepView for a toy example. Step 1: Data set (left) is projected to two dimensions with UMAP (middle). Step 2: The created regular grid is depicted with green crosses (middle) and the result of  $\pi^{-1}$  is depicted with green dots (right). Step 3: The predictions of the model can now be obtained (right). Step 4: Visualization of the prediction for the grid points is depicted in the background, where the entropy of the predictive distribution is given by the intensity (middle).

since there do not exist homeomorphic mappings in between topological spaces of different dimensionality. A key challenge is how to efficiently and effectively determine a regularization and which aspects of the data space need to be displayed. In this contribution, we will build on the rich work of non-linear dimensionality reduction techniques, in particular the recent methodology UMAP, which is mathematically substantiated by a clear topological motivation, and we propose a pipeline *DeepView*, how to display deep networks decision functions for trained networks and benchmark training data. To do so, we introduce two central ingredients: (i) we propose a novel discriminative variant of UMAP, which takes into account the information relevant for a priorly trained deep network, and we propose a mathematically sound method how to compute this information efficiently. (ii) Further, we propose a novel way how UMAP can be enriched to also provide an "inverse" mapping, which abstracts from information, which is not relevant for the deep network (an exact inverse cannot exist, obviously). (iii) We demonstrate the effectiveness of the new visualization pipeline *DeepView* for popular deep learning models and data sets.

## 2 DeepView: visualizing the decision function of a deep network

In the trivial case of two-dimensional data, the visualization of a trained classification model is a straightforward and useful thing: we can apply the classifier to each position in a certain area around our data and encode the predicted label and the according certainty in the background of a scatter plot. This illustrates very clearly how the trained model behaves in each area of the data space.

For high-dimensional data, however, this is not directly possible for several reasons: (i) While we can apply dimensionality reduction to project data for visualization, regular DR techniques will try to preserve all the structure in the data and, such, make critical compromises, for instance preserving brightness differences instead of object relevant properties, in the case of images. (ii) The classifier is usually trained in a high-dimensional space. Hence, applying it to every position in the data space is not feasible because of an exponentially growing number of positions. (iii) Finally, visualizing a full high-dimensional classifier in two dimensions is not possible because the decision function is high-dimensional and a projection of it (if possible at all) would yield drastic information loss.

## 2.1 DeepView: proposed visualization scheme

In this contribution, we develop a scheme that enables us to circumvent these problems and propose feasible approximations for the case of deep neural network classifiers. In particular, we propose to use discriminative dimensionality reduction based on the trained classification model 3.1, enabling the DR to focus the aspects of the data which are relevant for the classifier, alleviating problem (i). Further, instead of trying to obtain predictions for the full data space, we develop a scheme to obtain predictions only for a relevant subspace which we then use to visualize the decision function in two dimensions, such, solving problem (ii) and tackling problem (iii) by a reasonable approximation. This is based on inverse dimensionality reduction and is modeled in such a way that it matches the way the DR is constructed 3.2.

We propose to apply the following steps:

1. Apply the discriminative DR technique Fisher UMAP (developed in section 3.1) which is based on the underlying deep network to project a data set consisting of points  $\mathbf{x}_i$  to two dimensions, yielding  $\mathbf{y}_i = \pi(\mathbf{x}_i)$ .
2. Create a tight regular grid of samples  $\mathbf{r}_i$  in the two-dimensional space and map it to the high-dimensional space using the similarity coordinate embedding approach presented in section 3.2, yielding points  $\mathbf{s}_i = \pi^{-1}(\mathbf{r}_i)$ .
3. Apply the neural network  $f$  to  $\mathbf{s}_i$  in order to obtain predictions and certainties.
4. Visualize the label together with the entropy of the certainty for each position  $\mathbf{r}_i$  in the background of the projection space in order to obtain an approximation of the decision function.

These steps are demonstrated on a toy example in Figure 1. A similar scheme was employed in [22], but with choices of  $\pi$  and  $\pi^{-1}$  that restricted its application to data with up to 30 dimensions (enforced with a PCA preprocessing).

## 2.2 Evaluation of an obtained visualization

The previous section presents our new approach to investigate in how far a trained deep network can be trusted. Before it can be applied, however, it is important to investigate how accurate this visualization is. Here, two questions need to be answered: (I) how well does  $\pi$  show the view of the classifier on the data and (II) how well is  $\pi^{-1}$  depicting the decisions of the classifier in these areas?

In order to answer question (I), we pursue the following intuition: If the projection  $\pi$  takes the decision function of the classifier properly into account, then the classification decisions should be partially represented in the structure of the projected data points. I.e. points that are close to each other should be points that are classified similarly by the classification model. We can verify the degree to how much this is true by evaluating the accuracy of a simple classifier trained in the projection space using the labels of the deep network. For this purpose, we utilize the leave-one-out error of a  $k$ -nearest neighbor (kNN) classifier with  $k = 5$  being a standard choice and refer to this measure as  $Q_{\text{kNN}}$ . When we consider UMAP based on the Euclidean metric, we denote this measure as  $Q_{\text{kNN-E}}$ .

(II) Evaluating  $\pi^{-1}$  is less straight-forward. Here we suggest a scheme to evaluate the quality of the depicted decision function on the positions of the data points. For every point  $\mathbf{y}_i$ , compare the classification label of its original counterpart and the classification label of its inverse projection. More formally, we calculate the accordance of  $f(\pi^{-1}(\mathbf{y}_i))$  and  $f(\mathbf{x}_i)$ . Depending on the selected points, such an evaluation will have different implications: Using those point pairs  $(\mathbf{x}_i, \mathbf{y}_i)$  that have been employed to train the mapping  $\pi^{-1}$  will result in an assessment of the quality at the positions of the data points. Using point pairs that have not been utilized for training  $\pi^{-1}$  will rate the quality of the mapping at positions not seen before, i.e. of areas without data. Both are useful since they tell us how accurate the visualization is in areas where data points are available and in those where this is not the case. We will refer with  $Q_{\text{data}}$  to the former and with  $Q_{\text{-data}}$  to the latter.

### 3 Dimensionality reduction

Dimensionality reduction techniques for visualization aim to find mappings  $\pi : (S, d_S) \rightarrow \mathbb{R}^d, d = 2, 3$ , where  $(S, d_S)$  is some metric space, such that  $\pi$  preserves the information encoded in a set of data points  $\mathbf{x}_1, \dots, \mathbf{x}_n \in S$  as good as possible. The main aspect of a dimensionality reduction method is therefore to find a measure, and hence a cost function, to compare the information contained in two sets of points, allowing us to find a set of points  $\mathbf{y}_1, \dots, \mathbf{y}_n \in \mathbb{R}^d, d = 2, 3$  encoding the nearby same information. While the state of the art approach for performing nonlinear DR is t-Distributed Stochastic Neighbor Embedding (t-SNE) [24], recently a novel technique has been developed called Uniform Manifold Approximation and Projection (UMAP) [15] which produces at least comparable results to t-SNE and is formulated in a way that we make use of for our inverse projection  $\pi^{-1}$ . Hence, we focus on UMAP in the remaining of this manuscript.

Since the inverse projection map  $\pi^{-1}$  we will develop in the following is closely related to UMAP let us first recall the method: UMAP assumes that data is distributed according to a uniform distribution on a Riemannian manifold which may be approximated by a simplicial complex. The main structure is hence given by the topological features of that manifold. Thereby, we recall that a simplicial complex consists of a set of point (the 0-skeleton) and their connections, i.e. edges (1-skeleton), planes (2-skeleton) and hyper planes between them. Though we are not aware of the actual complex we may still estimate the probability for a certain  $n$ -simplex to exist. This way we may obtain simplicial complex valued random variables for any set of points in a metric space. Since we may compare those random variables using Kullback-Leibler divergence we obtain cost function.

To find the low dimensional embedding, the problem is restricted to the complex's 1-skeleton, i.e. the probability that two points are connected by an edge. It is assumed that the probability of an edge is induced by the distance between the end points and the local density. In the embedding space  $(\mathbb{R}^d, d = 2, 3)$  this is modeled by a student-t-distribution  $w_{ij} = (1 + a\|\mathbf{y}_i - \mathbf{y}_j\|^{2b})^{-1}$ , where  $a$  and  $b$  are hyper parameters, in the original space  $(S, d_S)$  one uses  $v_{ij} = v_{i|j} \perp v_{j|i}$ , where  $x \perp y = x + y - xy$  is the sum T-conorm and  $v_{i|j} = \exp(-\max(d(\mathbf{x}_i, \mathbf{x}_j)^2 - \rho_i, 0)/\sigma_i)$ , with  $\sigma_i$  the  $k$ -perplexity at  $\mathbf{x}_i$  and  $\rho_i = \min_{i \neq j} d(\mathbf{x}_i, \mathbf{x}_j)^2$  the distance to the nearest neighbor.

One then finds  $\mathbf{y}_i \in \mathbb{R}^d, i = 1, \dots, n, d = 2, 3$  by minimizing the Kullback-Leibler divergence of the embedding given the data, i.e.

$$\operatorname{argmin}_{\mathbf{y}_1, \dots, \mathbf{y}_n} \sum_{i \neq j} D_{\text{KL}}(v_{ij} \| w_{ij}) = \operatorname{argmin}_{\mathbf{y}_1, \dots, \mathbf{y}_n} \sum_{i \neq j} v_{ij} \log w_{ij} + (1 - v_{ij}) \log(1 - w_{ij})$$

#### 3.1 Discriminative dimensionality reduction

While DR methods are capable of preserving the structure to a large degree, they still have to make compromises if the structure is intrinsic too complex. Imagine for instance, a filled three-dimensional ball, which is impossible to embed accurately in two dimensions. A promising solution in this problem is the class of discriminative dimensionality reduction (DiDi) methods. These particularly focus on the structure important for a given classification task [25, 6] and such provide a specification which structure is more important than other. In our setting, we are given a classifier  $f$  on a set  $S$  (e.g.  $S = \mathbb{R}^D, D \gg d$ ) which we want to visualize. Hence, a natural choice is to visualize (sample) points with respect to  $f$  by choosing a metric  $d_S$  that does only depend on  $f$  and the topology of  $S$ .

Let  $S$  be our sample space and  $\mathcal{C}$  be our target space, e.g. the collection of all class labels. Then we may consider a classifier as a map  $f : S \rightarrow \mathcal{P}(\mathcal{C})$  that maps every point onto its class probabilities.

A first approach to define  $d_S$  is to choose a metric  $d_{\mathcal{P}}$  on  $\mathcal{P}(\mathcal{C})$  and then use the pullback  $f^*d_{\mathcal{P}}(x, y) = d_{\mathcal{P}}(f(x), f(y))$ . Obviously this will have the pleasant property that points with a nearby equivalent assignment will be considered as very close. However we will also eliminate all topological properties of  $S$

since points that are mapped to the same class will be considered as the same, no matter where they are in the sample space; even if they are separated by a second class. To overcome this problem we may use the arc length metric induced by  $f^*d_{\mathcal{P}}$ , i.e. instead of measuring the distance between two points  $x, y \in S$  directly we measure the length of the shortest continuous curve  $\gamma : [0, 1] \rightarrow S$  starting at  $x = \gamma(0)$  and ending at  $y = \gamma(1)$ , where the length of  $\gamma$  is given by

$$L_d(\gamma) = \sup_{0=t_0 < \dots < t_n=1} \sum_{i=1}^n d(\gamma(t_{i-1}), \gamma(t_i)).$$

We will denote such a metric by  $d_{L_d}$ . Note that  $d_{L_{f^*d_{\mathcal{P}}}}$  still considers points as equal if and only if we may find path where  $f$  is constant, so only connected regions with constant class probabilities are collapsed to a single point. However if  $(S, d'_S)$  is already a metric space it may be reasonable to regularize with  $d'_S$ , i.e. we may choose  $d_S$  as the arc length metric over  $f^*d_{\mathcal{P}} + \lambda d'_S$  for some  $\lambda > 0$  instead. This is also beneficial for two reasons: first it enforces  $d_S$  to be a metric and secondly it enforces the minimal curves to stay near by.

Therefore it remains to choose a metric on  $\mathcal{P}(\mathcal{C})$ : A first guess could be the Kullback-Leibler divergence  $D_{\text{KL}}$ , however it is not a metric though. By symmetrizing and smoothing we can obtain the Jensen-Shannon divergence  $D_{\text{JS}}(P \| Q) := \frac{1}{2} (D_{\text{KL}}(P \| M) + D_{\text{KL}}(Q \| M))$ , where  $M = \frac{P+Q}{2}$ , which is a squared metric indeed, i.e.  $\sqrt{D_{\text{JS}}}$  is a metric.

In order to implement this approach one may approximate  $d_S$  by

$$d_S(x, y) = d_{L_{f^*\sqrt{D_{\text{JS}}} + \lambda d'_S}}(x, y) \stackrel{\approx}{\approx} L_{f^*\sqrt{D_{\text{JS}}} + \lambda d'_S}(\gamma_{x,y}),$$

$$\sum_{i=1}^n \sqrt{D_{\text{JS}}(f(p_{n,i-1}) \| f(p_{n,i})) + \lambda d'_S(p_{n,i-1}, p_{n,i})} \xrightarrow{n \rightarrow \infty} L_{f^*\sqrt{D_{\text{JS}}} + \lambda d'_S}(\gamma_{x,y}),$$

where  $p_{n,i} = \gamma_{x,y}(\frac{i}{n})$  and  $\gamma_{x,y}$  is the assumed shortest path from  $x$  to  $y$ , with the approximation  $\gamma_{x,y}(t) = tx + (1-t)y$ .

Furthermore note that the arc length metric induced by  $f^*\sqrt{D_{\text{JS}}}$  is (up to an factor of  $\sqrt{8}$ ) equivalent to the Fisher-metric, which is widely used in information geometry (see [3, 2]) where it is defined via a metric tensor. While in [3, 2] the Fisher-metric is defined in the parameter space of a model, here we use it in the data space directly, as suggested in [10, 18]. In particular we see that the Fisher metric arises naturally in the setup of discriminative dimensionality reduction. Furthermore it was evaluated in [18] that the straight line approximation of  $\gamma$  is sensible. Note however that our approach is, in particular for deep networks, far more efficient than the techniques proposed in [18] using the Fisher matrix directly, since we only have to do a forward propagation, rather than a back propagation.

### 3.2 Similarity coordinate embedding for inverse dimensionality reduction

So far we have discussed the task of finding a mapping  $\pi : (S, d_S) \rightarrow \mathbb{R}^d, d = 2, 3$ . Now we are interested in finding a map  $\pi^{-1}$  such that  $\mathbb{E}[d_S(\pi^{-1} \circ \pi(X), X)^2] \approx 0$ , where  $X$  is a  $S$ -valued random variable which is distributed according to our data. We would like to obtain  $\pi^{-1}$  in a particular natural way, under the assumption that  $\pi$  is given by UMAP.

To do so assume we are given a metric space  $(S, d_S)$  and points  $\mathbf{x}_1, \dots, \mathbf{x}_n \in S$ . We obtain a mapping  $c_S : S \rightarrow \mathbb{R}^n, \mathbf{s} \mapsto (d_S(\mathbf{x}_1, \mathbf{s}), \dots, d_S(\mathbf{x}_n, \mathbf{s}))$ . If we assume that  $(S, d_S) = (\mathbb{R}^{n-1}, \|\cdot\|_2)$  then this is closely related to barycentric coordinates. We may also do the same thing for a second space  $(R, d_R)$  and obtain  $c_R : R \rightarrow \mathbb{R}^n$ . This allows us to compare  $\mathbf{s} \in S$  and  $\mathbf{r} \in R$  by simply defining an equivalence measure  $D$  on  $\mathbb{R}^n$ . Note that this still works if we apply some mappings  $g_S, g_R : \mathbb{R}^n \rightarrow \mathbb{R}^{n'}$  beforehand if the chosen mappings are "injective enough".

One way to choose  $g_S$  is such that  $\mathbf{s} \mapsto (g_S \circ c_S(\mathbf{s}))_i$  is a similarity measure with respect to  $\mathbf{x}_i$ . We will refer to this as similarity coordinates. Indeed both UMAP and t-SNE may be described in this

framework, where  $g_S$  and  $g_R$  are basically given by (symmetrized normalizations of) similarity coordinates, e.g.  $g_R \circ c_R(\mathbf{y}_i) = (w_{i1}, \dots, w_{in})$ ,  $g_S \circ c_S(\mathbf{x}_i) = (v_{i1}, \dots, v_{in})$  and  $D$  is given by the Kullback-Leibler divergence.

Our next step towards  $\pi^{-1}$  is to choose  $g_R$  and  $g_S$ . We do so by defining  $w_i(\mathbf{r}) := (1 + ad_R(\mathbf{r}, \rho_i)^{2b})^{-1}$ ,  $p_i(\mathbf{r}) = (w_i(\mathbf{r}), 1 - w_i(\mathbf{r}))$  and  $v_i(\mathbf{s}) = \exp(-d_S(\mathbf{s}, \theta_i)^2/\sigma_i)$ ,  $q_i(\mathbf{s}) = (v_i(\mathbf{s}), 1 - v_i(\mathbf{s}))$ , where  $a$  and  $b$  are hyper parameters and  $\rho_i, \theta_i$  and  $\sigma_i$  are estimated to minimize the projection error. Thus we obtain:

$$\pi^{-1}(\mathbf{r}) := \operatorname{argmin}_{\mathbf{s} \in S} \sum_{i=1}^n D_{\text{KL}}(p_i(\mathbf{r}) || q_i(\mathbf{s})) = \operatorname{argmin}_{\mathbf{s} \in S} \sum_{i=1}^n H(p_i(\mathbf{r}); q_i(\mathbf{s})) = \operatorname{argmin}_{\mathbf{s} \in S} H(\mathbf{r}; \mathbf{s}) \quad (1)$$

$$H(\mathbf{r}; \mathbf{s}) := \sum_{i=1}^n H(p_i(\mathbf{r}); q_i(\mathbf{s})) = - \sum_{i=1}^n w_i(\mathbf{r}) \log v_i(\mathbf{s}) + (1 - w_i(\mathbf{r})) \log(1 - v_i(\mathbf{s})) \quad (2)$$

In the following let us fix  $R = \mathbb{R}^d$ ,  $d = 2, 3$  with the euclidean metric. Since the further steps depend heavily on  $(S, d_S)$  we may only consider two examples in more detail:

Supposing that  $(S, d_S) = (\mathbb{R}^D, \|\cdot\|_2)$  with  $d \ll D$ . Though we may simply apply some optimization methods, it is reasonable to first consider eq. 2 a bit more closely: Since the euclidean metric suffers from the curse of dimension and  $\exp(-\cdot^2/\sigma)$  is quite sharp it is reasonable to assume  $-\sum_i (1 - w_i(\mathbf{r})) \log(1 - v_i(\mathbf{s})) \approx 0$ . Then by computing derivative and setting zero we obtain  $\pi^{-1}(\mathbf{r}) \approx (\sum_{i=1}^n w_i(\mathbf{r})/\sigma_i)^{-1} \sum_{i=1}^n w_i(\mathbf{r})/\sigma_i \cdot \mathbf{x}_i$  (See the supplemental materials for details). Therefore we may consider  $\pi^{-1}$  as a kind of radial basis-function network and we may speed up our computation by considering neighbors of  $\mathbf{r}$  only. In this case however we must not simply use the  $k$  nearest neighbors, a suitable technique based on Delaunay triangulation is presented in the supplemental material, and a smoothing operation is needed to avoid discontinuities in the resulting manifold.

To generalize this approach to arbitrary Riemannian manifolds recall that those are locally, approximately given by inner product spaces. It is therefore enough to generalize our approach to arbitrary, finite dimensional, inner product spaces, i.e.  $(S, d_S) = (S, \|\cdot\|_S)$ , where  $\|v\|_S = \sqrt{\langle v, v \rangle_S}$ :

**Lemma 1.** *Let  $S$  be a finite dimensional real vector space. Let  $d : S \times S \rightarrow \mathbb{R}$  be a metric induced by an inner product and  $X$  be a  $S$ -valued random variable. Then it holds  $\operatorname{argmin}_{x \in S} \mathbb{E}[d(X, x)^2] = \operatorname{argmin}_{x \in S} \mathbb{E}[\|X - x\|_S^2]$ .*

We prove this lemma in the supplemental materials. So if we consider a Riemannian manifold  $(M, d_M)$  and we approximate  $d_M$  at  $\mathbf{s}^*$ , the point we are searching for, we obtain the same formula as in the euclidean case.

**Training  $\pi^{-1}$**  To find  $\pi^{-1}$  such that  $\mathbb{E}[d_S(\pi^{-1} \circ \pi(X), X)^2] \approx 0$  we need to estimate  $\rho_i, \theta_i$  and  $\sigma_i$  given samples  $\mathbf{x}_i$  and their projection  $\pi(\mathbf{x}_i) = \mathbf{y}_i$ . We may choose  $\rho_i = \mathbf{y}_i$  and  $\sigma_i$  as the local perplexity (cf. [15] or [24] respectively). Then we choose  $\theta_i$  such that  $\mathbb{E}[d_S(\pi^{-1} \circ \pi(X), X)^2]$  is minimized. We may write  $\pi^{-1}(\mathbf{r}) = \Theta w(\mathbf{r})$ , where  $\Theta = (\theta_1, \dots, \theta_n)$  is a  $\mathbb{R}^{D \times n}$ -matrix and  $w(\mathbf{r})$  is the  $\mathbf{r}$ -dependent, normalized weighting vector induced by  $w_i(\mathbf{r})/\sigma_i$ . By approximating  $d_S$  locally by  $A_i = g(\mathbf{x}_i)$ , where  $g$  is the metric tensor of our manifold, we obtain the gradient as

$$J(\Theta) = \nabla_{\Theta} \sum_{i=1}^n (\Theta w(\mathbf{y}_i) - \mathbf{x}_i)^t A_i (\Theta w(\mathbf{y}_i) - \mathbf{x}_i) = \sum_{i=1}^n A_i (\Theta w(\mathbf{y}_i) - \mathbf{x}_i) w(\mathbf{y}_i)^t$$

We may therefore minimize the error using gradient descent, starting at  $\Theta = (\mathbf{x}_1, \dots, \mathbf{x}_n)$ . Note that we may compute the optimal learning rate  $\eta_{\text{opt}}(J, \Theta)$  (See the supplemental materials for details). Furthermore It turned out that using a momentum  $\gamma \in [0, 1)$  is suitable. It also turned out to be suitable to run a few iterations using euclidean metric before using the actual desired metric (this is sensible since we only have  $d_S(x, y)^2 \approx (x - y)^t A_i (x - y)$  in some neighborhood of  $\mathbf{x}_i$ ).

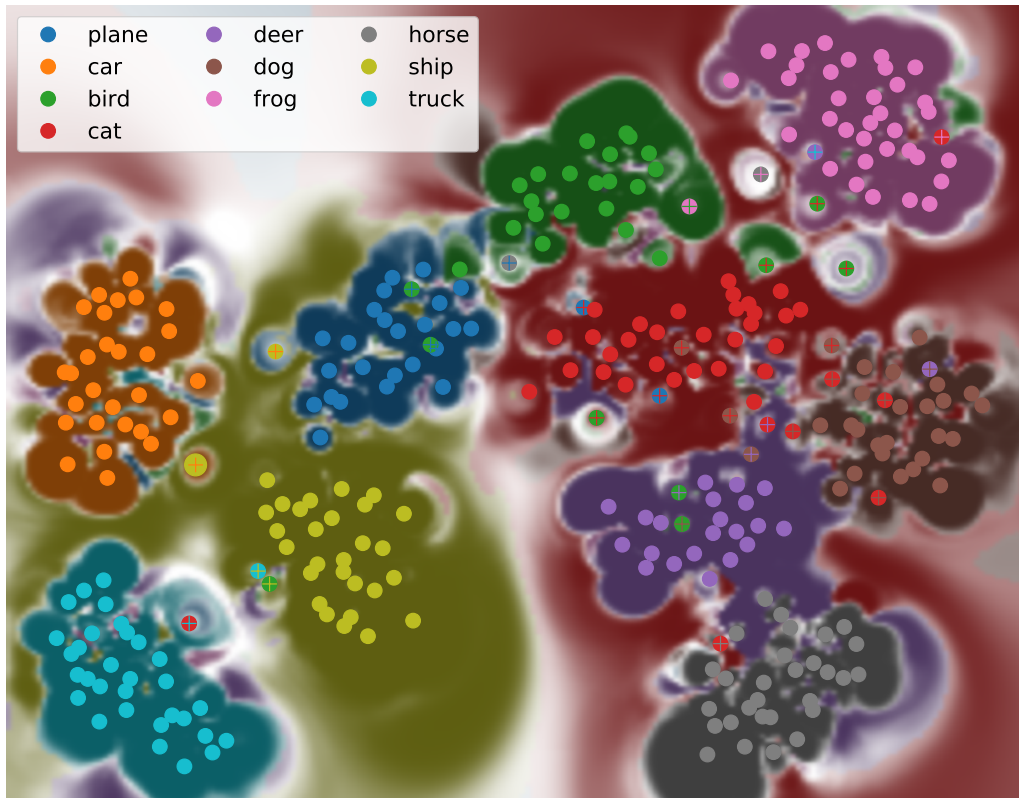


Figure 2: Visualization of a ResNet-20 model trained on the CIFAR-10 data set together with a subset of the test data. The big orange yellow circle depicts an adversarial example.

## 4 Experiments

In this section we apply the proposed method DeepView to visualize classifiers trained on the datasets CIFAR-10 and ImageNet. In both cases, we employ popular pre-trained deep networks and inspect their decision function together with a part of the data set. We evaluate the resulting visualizations with the scores  $Q_{\text{kNN}}$ ,  $Q_{\text{data}}$ ,  $Q_{\text{-data}}$  as discussed in section 2.2, where we use 70% for training in  $Q_{\text{-data}}$ .

For DR we approximate the Fisher metric using the symmetrized local KL divergence and regularize it with the Euclidean metric as described in section 3.1. We choose the amount of Euclidean regularization in the following way: we evaluate  $\pi$  with  $Q_{\text{kNN}}$  using different values of  $\lambda$  and choose the largest one that does not degrade  $Q_{\text{kNN}}$  significantly. For estimating  $\pi^{-1}$  we did not observe large improvements under the Fisher metric and hence utilize the Euclidean metric for more efficiency. Note that the Fisher metric is essential for estimating  $\pi$ , as we will show. Here we set  $a$  to the smallest value that does not lead to a large drop in  $Q_{\text{data}}$  and  $b = 1$ .

### 4.1 Visualizing a ResNet-20 network trained on the CIFAR-10 dataset

The *CIFAR-10 data set* consists of 32x32 color images containing 10 different classes (see Figure 2 for the list). The training set contains 50.000 examples and present implementation has an accuracy of 91.7% on the 10.000 test images.

For this data set we utilize the pre-trained residual network (ResNet) with 20 layers described in [8].<sup>1</sup>

The result of DeepView applied to a subset of 300 points selected randomly from the test set and the ResNet-20 network is shown in Figure 2. Each point corresponds to one image and the color indicates its original label. If classified differently by the deep net, a cross in the according color indicates that label. The color of the background depicts the classification of the net in that are and the intensity encodes the certainty.

First of all, we consider the evaluation of the resulting visualization and, second, discuss the information than can be drawn from it. The former are summarized in Table 1. For the sake of completeness, we also evaluate the UMAP projection based on the Euclidean metric ( $Q_{\text{kNN-E}}$ ). The accuracy in this case amounts to 18.9%, which makes clear that such an embedding is not useful in this case. With the Fisher metric, however, the accuracy is 97% indicating that the projection space very well resembles the classification behavior of our model. Concerning the visualization of the decision function, the close to perfect  $Q_{\text{data}}$  demonstrates that the visualization is very accurate at the given data points. For the vicinity of the data points,  $Q_{\text{-data}}$  asses an accuracy 82.2%.

Regarding the visualization, the decision boundaries for the class 'orange' seem to have the most complex shape, indicating that this class might be particularly difficult. Indeed, when inspecting the confusion matrix, this class has the smallest true positive rate with 83.2%. Furthermore, we can identify several points that are treated specially. One example is the yellow point that we have depicted with a larger symbol. This constitutes an adversarial example that we have created using the sign of the model gradient [7] and have added to the 300 images. The visualization shows how this point is classified as orange by the classifier, but this area is surrounded by the yellow class. Since this seems interesting, we take a closer look, by zooming into the according area (see Figure 3, left). Since this visualization is constructed by an inverse mapping, we can inspect images according to arbitrary positions in the visualization. In order to do so, we specify potentially interesting positions in the vicinity of the adversarial example (see 3, left) and depict their projections with  $\pi^{-1}$  on the right side. The markers '0', '1', and '2' are in the area of the yellow class which encodes ships and the according images can be clearly identified as such. Although the images of the markers '2', '3', '4' and '5' look fairly similar, their classifications vary heavily, going from 'ship' to 'car' and back to 'ship'. These images show, that there seems to be a kind of 'pocket' of the 'car' class inside the 'ship' class while the images in this pocket still look like natural ships to a human. This concept of 'pockets'

<sup>1</sup>We employ the implementation from [https://github.com/akamaster/pytorch\\_resnet\\_cifar10](https://github.com/akamaster/pytorch_resnet_cifar10).



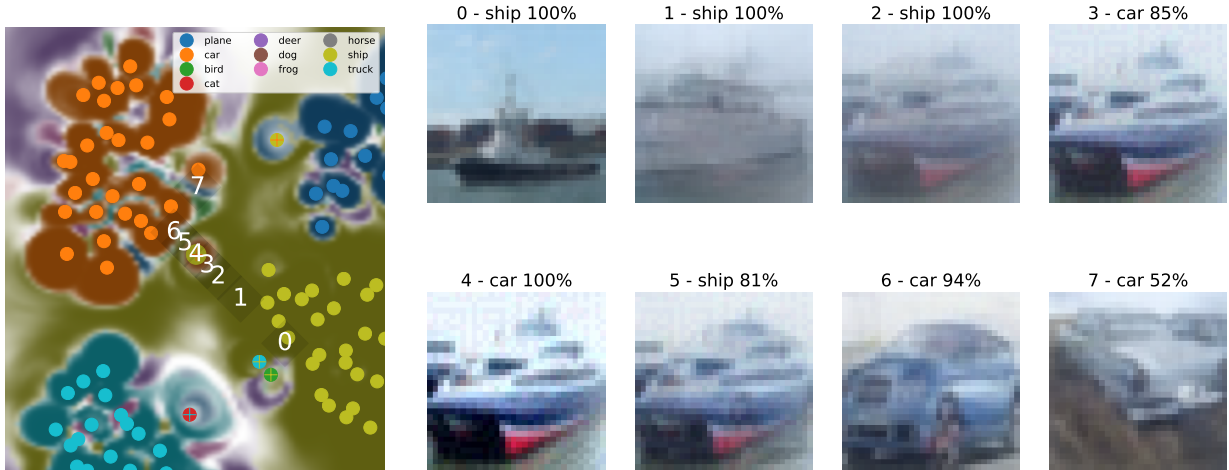


Figure 3: A zoomed in view on Figure 2 together with markers of specified positions around the adversarial example (left). The resulting images of the inverse mapping  $\pi^{-1}$  for the previously specified positions, together with the assigned label and according certainty of the classifier (right).

Table 1: Results of different evaluation criteria defined in section 2.2, characterizing the quality of the embeddings.  $Q_{\text{kNN-E}}$  is calculated on a UMAP embedding based on the Euclidean metric. For the other scores, Fisher UMAP mappings only are considered.

Data Set	$Q_{\text{kNN-E}}$	$Q_{\text{kNN}}$	$Q_{\text{data}}$	$Q_{\text{-data}}$
CIFAR-10	21.6%	97.0%	99.7%	82.2%
ImageNet	39.5%	79.1%	90.7%	54.4%

has been addressed in the literature before [5]. Interestingly, the closest area of the 'orange' class marked with '6' is again clearly a 'car' which looks from a broad view (orientation of the object as well as color and background) very similar to our adversarial ship.

As a further example, another point classified as 'orange' is lying in an 'orange island' area near the marker '7'. The projected image looks clearly like a car but is classified rather uncertainly. This seems to be another area, where the classifier behaves in an unclear way and might use intervention (e.g. more training data).

These were a few examples of how we could deduce useful information from a DeepView visualization. We provide the visualization of the AlexNet model for ImageNet in the supplement materials.

## 5 Conclusion

In this work we propose *DeepView*, to the best of our knowledge the first algorithm that is able visualize the decision function of a deep neural network which is trained on high-dimensional data such as natural images. For this purpose, we adopt a mathematically precise formulation of discriminative DR together with a matching choice of inverse DR. We apply DeepView to two deep networks from the literature, a Residual Network with 20 layers trained on CIFAR-10 and the AlexNet trained on ImageNet, and demonstrate how it provides insight into the model and data domain.

While we demonstrate DeepView only for image data in this article, the method is no way restricted to this domain and applications to text analysis and other areas constitute interesting further application areas. An interesting open question in that regard is how to extend the utilized Fisher metric in case of e.g. temporal data.

We believe that the presented approach can not only provide insights into trained models but in this way also contribute to improve these models, by e.g. providing insights into areas of lacking data.

## Acknowledgments

Funding by the CITEC center of excellence (EXC 277) and from BMBF within the project MechML under grant number 01IS18053E is gratefully acknowledged.

## References

- [1] D. Alvarez-Melis and T. S. Jaakkola. A causal framework for explaining the predictions of black-box sequence-to-sequence models. *CoRR*, abs/1707.01943, 2017.
- [2] S. Amari and H. Nagaoka. *Methods of Information Geometry*. Translations of mathematical monographs. American Mathematical Society, 2007.
- [3] S.-i. Amari. Differential-geometrical methods in statistics. *Lecture Notes on Statistics*, 28:1, 1985.
- [4] G. F. Elsayed, S. Shankar, B. Cheung, N. Papernot, A. Kurakin, I. J. Goodfellow, and J. Sohl-Dickstein. Adversarial examples that fool both human and computer vision. *CoRR*, abs/1802.08195, 2018.
- [5] R. Feinman, R. R. Curtin, S. Shintre, and A. B. Gardner. Detecting adversarial samples from artifacts. *arXiv preprint arXiv:1703.00410*, 2017.
- [6] A. Gisbrecht, A. Schulz, and B. Hammer. Parametric nonlinear dimensionality reduction using kernel t-sne. *Neurocomputing*, 147:71 – 82, January 2015. Advances in Self-Organizing Maps Subtitle of the special issue: Selected Papers from the Workshop on Self-Organizing Maps 2012 (WSOM 2012).
- [7] I. J. Goodfellow, J. Shlens, and C. Szegedy. Explaining and harnessing adversarial examples. *arXiv preprint arXiv:1412.6572*, 2014.
- [8] K. He, X. Zhang, S. Ren, and J. Sun. Deep residual learning for image recognition. In *Proceedings of the IEEE conference on computer vision and pattern recognition*, pages 770–778, 2016.
- [9] M. Jagielski, A. Oprea, B. Biggio, C. Liu, C. Nita-Rotaru, and B. Li. Manipulating machine learning: Poisoning attacks and countermeasures for regression learning. In *2018 IEEE Symposium on Security and Privacy (SP)*, pages 19–35, May 2018.
- [10] S. Kaski, J. Sinkkonen, and J. Peltonen. Bankruptcy analysis with self-organizing maps in learning metrics. *IEEE Transactions on Neural Networks*, 12:936–947, 2001.
- [11] A. Krizhevsky, I. Sutskever, and G. E. Hinton. Imagenet classification with deep convolutional neural networks. In *Advances in neural information processing systems*, pages 1097–1105, 2012.
- [12] I. Lage, E. Chen, J. He, M. Narayanan, B. Kim, S. Gershman, and F. Doshi-Velez. An evaluation of the human-interpretability of explanation. *CoRR*, abs/1902.00006, 2019.
- [13] S. Leavy. Gender bias in artificial intelligence: The need for diversity and gender theory in machine learning. In *2018 IEEE/ACM 1st International Workshop on Gender Equality in Software Engineering (GE)*, pages 14–16, May 2018.
- [14] V. Losing, B. Hammer, and H. Wersing. Tackling heterogeneous concept drift with the self-adjusting memory (SAM). *Knowl. Inf. Syst.*, 54(1):171–201, 2018.
- [15] L. McInnes, J. Healy, and J. Melville. Umap: Uniform manifold approximation and projection for dimension reduction. *arXiv preprint arXiv:1802.03426*, 2018.
- [16] J. Montiel, J. Read, A. Bifet, and T. Abdesslem. Scikit-multiflow: A multi-output streaming framework. *Journal of Machine Learning Research*, 19:72:1–72:5, 2018.
- [17] S. T. Mueller, R. R. Hoffman, W. J. Clancey, A. Emrey, and G. Klein. Explanation in human-ai systems: A literature meta-review, synopsis of key ideas and publications, and bibliography for explainable AI. *CoRR*, abs/1902.01876, 2019.

- [18] J. Peltonen, A. Klami, and S. Kaski. Improved learning of riemannian metrics for exploratory analysis. *Neural Networks*, 17:1087–1100, 2004.
- [19] M. T. Ribeiro, S. Singh, and C. Guestrin. Anchors: High-precision model-agnostic explanations. In *Proceedings of the Thirty-Second AAAI Conference on Artificial Intelligence, (AAAI-18), the 30th innovative Applications of Artificial Intelligence (IAAI-18), and the 8th AAAI Symposium on Educational Advances in Artificial Intelligence (EAAI-18), New Orleans, Louisiana, USA, February 2-7, 2018*, pages 1527–1535, 2018.
- [20] W. Samek, T. Wiegand, and K. Müller. Explainable artificial intelligence: Understanding, visualizing and interpreting deep learning models. *CoRR*, abs/1708.08296, 2017.
- [21] B. Scholkopf and A. J. Smola. *Learning with Kernels: Support Vector Machines, Regularization, Optimization, and Beyond*. MIT Press, Cambridge, MA, USA, 2001.
- [22] A. Schulz, A. Gisbrecht, and B. Hammer. Using discriminative dimensionality reduction to visualize classifiers. *Neural Processing Letters*, 42(1):27–54, August 2015.
- [23] K. Sokol and P. Flach. Glass-box: Explaining ai decisions with counterfactual statements through conversation with a voice-enabled virtual assistant. In *Proceedings of the Twenty-Seventh International Joint Conference on Artificial Intelligence, IJCAI-18*, pages 5868–5870. International Joint Conferences on Artificial Intelligence Organization, 7 2018.
- [24] L. van der Maaten and G. Hinton. Visualizing high-dimensional data using t-sne. *Journal of Machine Learning Research*, 9:2579–2605, 2008.
- [25] J. Venna, J. Peltonen, K. Nybo, H. Aidos, and S. Kaski. Information retrieval perspective to nonlinear dimensionality reduction for data visualization. *Journal of Machine Learning Research*, 11:451–490, 2010.

## A Proofs and Algorithms

**Lemma 2.** *Let  $S$  be a finite dimensional real vector space. Let  $d : S \times S \rightarrow \mathbb{R}$  be a metric induced by an inner product and  $X$  be a  $S$ -valued random variable. Then it holds*

$$\operatorname{argmin}_{x \in S} \mathbb{E} [d(X, x)^2] = \operatorname{argmin}_{x \in S} \mathbb{E} [\|X - x\|_2^2].$$

*Proof.* Since  $d$  is induced by an inner product we may find a matrix  $A$  such that  $d(x, y)^2 = (x - y)^t A (x - y)$ .

**1. Case  $A$  is a diagonal matrix:** Then it holds

$$\mathbb{E} [d(X, x)^2] = \sum_i a_{ii} \mathbb{E} [(X_i - x_i)^2]$$

since we may optimize each component of  $x$  separately the statement follows.

**2. Case  $A$  is not diagonal:** Using the spectral theorem we obtain  $A = U^t D U$  (by spectral theorem we obtain  $A = V D V^t$  then we define  $U = V^t$ , since  $V$  is unitary so is  $U$ ), where  $D$  is a diagonal matrix and  $U$  is unitary. Hence it follows

$$\begin{aligned} \operatorname{argmin}_{x \in S} \mathbb{E} [d(X, x)^2] &= \operatorname{argmin}_{x \in S} \mathbb{E} [(U(X - x))^t D (U(X - x))] \\ &= \operatorname{argmin}_{x \in S} \mathbb{E} [(U X - U x)^t D (U X - U x)] \\ &= U^{-1} \operatorname{argmin}_{x' \in \operatorname{Im} U} \mathbb{E} [(U X - x')^t D (U X - x')] \\ &= U^{-1} \operatorname{argmin}_{x' \in \operatorname{Im} U} \mathbb{E} [\|U X - x'\|_2^2] && \text{1. Case} \\ &= \operatorname{argmin}_{x \in S} \mathbb{E} [\|U X - U x\|_2^2] \\ &= \operatorname{argmin}_{x \in S} \mathbb{E} [\|U(X - x)\|_2^2] \\ &= \operatorname{argmin}_{x \in S} \mathbb{E} [\|X - x\|_2^2]. && U \text{ is unitary} \end{aligned}$$

□

**Remark 1** (Derivation of  $\pi^{-1}$ ). *It holds*

$$\pi^{-1}(\mathbf{r}) := \operatorname{argmin}_{\mathbf{s} \in S} \sum_{i=1}^n D(p_i(\mathbf{r}) \| q_i(\mathbf{s})) \stackrel{!}{=} \operatorname{argmin}_{\mathbf{s} \in S} \sum_{i=1}^n H(p_i(\mathbf{r}); q_i(\mathbf{s}))$$

since  $\frac{\partial}{\partial \theta} D_{\text{KL}}(X \| f_\theta(Y)) = \frac{\partial}{\partial \theta} (H(X; f_\theta(Y)) - H(X)) = \frac{\partial}{\partial \theta} H(X; f_\theta(Y))$ , where  $H(\cdot)$  denotes entropy and  $H(\cdot; \cdot)$  denotes the cross entropy. Now by plugging in the definitions and approximations we obtain

$$\begin{aligned} H(\mathbf{r}; \mathbf{s}) &= - \sum_{i=1}^n w_i(\mathbf{r}) \log v_i(\mathbf{s}) - \underbrace{\sum_{i=1}^n (1 - w_i(\mathbf{r})) \log(1 - v_i(\mathbf{s}))}_{\approx 0} \\ &= - \sum_{i=1}^n w_i(\mathbf{r}) \left( - \frac{\|\mathbf{s} - \mathbf{x}_i\|_2^2}{\sigma_i} \right) \\ &= \sum_{i=1}^n \frac{w_i(\mathbf{r})}{\sigma_i} \|\mathbf{s} - \mathbf{x}_i\|_2^2 \\ \Rightarrow \nabla_{\mathbf{s}} H(\mathbf{r}; \mathbf{s}) &= 2 \sum_{i=1}^n \frac{w_i(\mathbf{r})}{\sigma_i} (\mathbf{s} - \mathbf{x}_i) \stackrel{!}{=} 0 \\ \Leftrightarrow \mathbf{s} &= \frac{\sum_{i=1}^n \frac{w_i(\mathbf{r})}{\sigma_i} \mathbf{x}_i}{\sum_{i=1}^n \frac{w_i(\mathbf{r})}{\sigma_i}}. \end{aligned}$$

Furthermore using the lemma above we see that

$$\begin{aligned}
\mathbf{s}^* &= \operatorname{argmin}_{\mathbf{s} \in S} - \sum_{i=1}^n w_i(\mathbf{r}) \log v_i(\mathbf{s}) \approx \operatorname{argmin}_{\mathbf{s} \in S} \sum_{i=1}^n \frac{w_i(\mathbf{r})}{\sigma_i} d_{s^*}(\mathbf{s}, \mathbf{x}_i)^2 \\
&= \operatorname{argmin}_{\mathbf{s} \in S} C \sum_{i=1}^n \frac{w_i(\mathbf{r})}{C} d_{s^*}(\mathbf{s}, \mathbf{x}_i)^2 = \operatorname{argmin}_{\mathbf{s} \in S} C \mathbb{E}_P [d_{s^*}(\mathbf{s}, X)^2] \\
&= \operatorname{argmin}_{\mathbf{s} \in S} C \mathbb{E}_P [\|\mathbf{s} - X\|^2] = \operatorname{argmin}_{\mathbf{s} \in S} C \sum_{i=1}^n \frac{w_i(\mathbf{r})}{C} \|\mathbf{s} - \mathbf{x}_i\|^2 \\
&= \frac{\sum_{i=1}^n \frac{w_i(\mathbf{r}) \mathbf{x}_i}{\sigma_i}}{\sum_{i=1}^n \frac{w_i(\mathbf{r})}{\sigma_i}},
\end{aligned}$$

where  $C = \sum_{i=1}^n \frac{w_i(\mathbf{r})}{\sigma_i}$ ,  $d_{s^*}$  the approximation of  $d_S$  at  $s^*$ ,  $X : \{1, \dots, n\} \rightarrow, i \mapsto \mathbf{x}_i$  a random variable and  $P(I) = \frac{1}{C} \sum_{i \in I} \frac{w_i(\mathbf{r})}{\sigma_i}$ .

**Lemma 3** (Derivation of  $\eta_{\text{opt}}$ ). *Let  $R, S$  be finite dimensional, real vector spaces. Let  $\mathbf{y}_i \in R, \mathbf{x}_i \in S, A_i \in \text{Mat}_{\mathbb{R}}(S, S)$ ,  $i = 1, \dots, n$  and  $\Theta, J \in \text{Mat}_{\mathbb{R}}(R, S)$ . Assume that  $A_i$  are symmetric and positive definite and denote by  $\|\cdot\|_i$  the induced norm, i.e.  $\|s\|_i := \sqrt{s^t A_i s}$ . Then it holds*

$$\operatorname{argmin}_{\eta} \sum_{i=1}^n \|(\Theta - \eta J) \mathbf{y}_i - \mathbf{x}_i\|_i^2 = \frac{\sum_{i=1}^n (\Theta \mathbf{y}_i - \mathbf{x}_i)^t A_i J \mathbf{y}_i}{\sum_{i=1}^n \mathbf{y}_i^t J^t A_i J \mathbf{y}_i}.$$

*Proof.* It holds

$$\begin{aligned}
\frac{d}{d\eta} \sum_{i=1}^n \|(\Theta - \eta J) \mathbf{y}_i - \mathbf{x}_i\|_i^2 &= 2 \sum_{i=1}^n ((\Theta - \eta J) \mathbf{y}_i - \mathbf{x}_i)^t A_i J \mathbf{y}_i \stackrel{!}{=} 0 \\
\Leftrightarrow \sum_{i=1}^n (\Theta \mathbf{y}_i - \mathbf{x}_i)^t A_i J \mathbf{y}_i &= \eta \sum_{i=1}^n \mathbf{y}_i^t J^t A_i J \mathbf{y}_i
\end{aligned}$$

□

## B Visualizing AlexNet for a subset of ImageNet

For our current experiments we utilize a subset of three classes from the full ImageNet data set,<sup>2</sup> the classes 'acoustic guitar', 'electric guitar' and 'grand piano'. As the pre-trained model we choose the popular AlexNet [11] and apply DeepView to 300 randomly selected data points and one adversarial example.

The resulting visualization is shown in Figure 4 with additional white circles around points for which the  $\pi^{-1}$  mapping is inaccurate (i.e. where  $Q_{\text{data}}$  counts mistakes). The evaluation is summarized in Table 1 and reveals lower scores as compared to the CIFAR-10 dataset. This is not surprising because the dataset, as well as the classifier (being trained on 1000 classes), is much more complex. Furthermore, the scores do not consider a top-5 measure as partially common with this dataset.

Concerning the visualization, we can observe that the 'piano' class is further away from the other two and that a set of points is classified as 'other' and is positioned in the middle. Again, the adversarial example is positioned outside of the main cluster and we investigate the area around it in the same as previously. While the position '0' is mapped to an image which is classified properly, the images of '1' to '5' are predicted with a high uncertainty and partially even wrong, although showing clearly guitars.

We select two further areas close to points being outside of their main cluster and mark them with '6' and '7'. This way we can get an impression why these images are classified incorrectly. In this case, the images show multiple objects with the target object being partially rather in the background.

<sup>2</sup><http://image-net.org/>

---

**Algorithm 1** Construction of Delaunay neighborhood

---

```
1: procedure CONSTRUCTDELAUNAYNEIGHBORHOOD( $(r_i)_{i=1,\dots,n}$  data points,  $n_s$  number of simplices,
    $n_k$  number of neighbors,  $\varepsilon$  minimal border distance)
2:    $C \leftarrow$  K-MEANS( $(r_i)_i, n_s$ )
3:    $B \leftarrow$  BORDER( $(r_i)_i, \varepsilon$ ) ▷ Vertices of a rectangle containing  $\cup_i B_{r_i}(\varepsilon)$ 
4:    $V \leftarrow C \cup B$  ▷ Assure that every  $r_i$  is actually contained in one simplex
5:    $S \leftarrow$  DELAUNAYTRIANGULATION( $V$ ) ▷ Delaunay triangulation for  $V$ , returns set of simplices
6:   for  $i \in [1, |S|]_{\mathbb{N}}$  do
7:      $V' \leftarrow$  GETVERTICES( $S_i$ ) ▷ Vertices of  $S_i$ 
8:     for  $j \in [1, D + 1]_{\mathbb{N}}$  do
9:        $\nu_j \leftarrow$  NEARESTNEIGHBORS( $(r_i)_i, V'_j, n_k$ ) ▷  $n_k$  nearest neighbors of  $V'_j$  in  $(r_i)_i$  sorted by
distance
10:      end for
11:       $N_i \leftarrow$  COMPOSENEIGHBORS( $\nu, n_k$ )
12:    end for
13:    return  $S, N$  ▷ Delaunay triangulation  $S$ , Delaunay neighborhood  $N$ 
14:  end procedure
15: procedure COMPOSENEIGHBORS( $(N_{ij})_{i=1,\dots,n, j=1,\dots,n_k}$  2d-array of nearest neighbors; row wise sorted
   by distance,  $n_k$  number of neighbors)
16:  for  $i \in [1, n]_{\mathbb{N}}$  do
17:     $k_i \leftarrow 0$ 
18:  end for
19:   $D \leftarrow \emptyset$  ▷ Use a heap for speedup
20:   $j \leftarrow 1$ 
21:   $i \leftarrow 1$ 
22:  while  $j \leq n_k$  do
23:     $k_i \leftarrow k_i + 1$ 
24:    if  $N_{ik_i} \notin D$  then ▷  $N_{ik_i}$  is not already contained in  $C$ 
25:       $D \leftarrow D \cup \{N_{ik_i}\}$ 
26:       $C_j \leftarrow N_{ik_i}$ 
27:       $i \leftarrow (i \bmod n) + 1$ 
28:       $j \leftarrow j + 1$ 
29:    end if
30:  end while
31:  return  $C$  ▷ composed neighborhood
32: end procedure
```

---

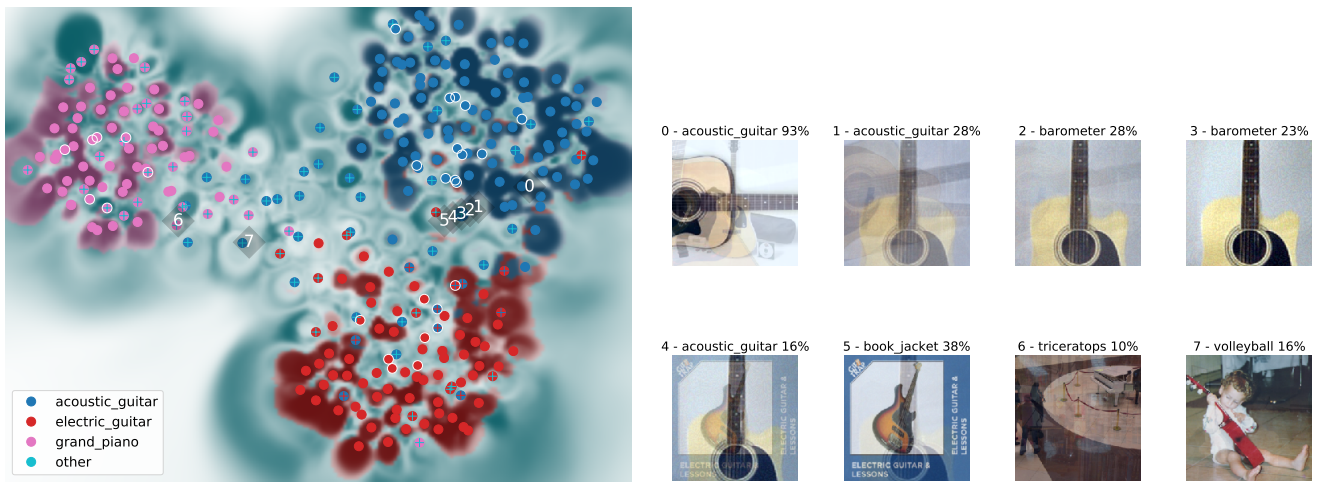


Figure 4: A visualization of a part of ImageNet and the AlexNet network together with markers of specified positions around the adversarial example (left). The resulting images of the inverse mapping  $\pi^{-1}$  for the previously specified positions, together with the assigned label and according certainty of the classifier (right).